



Cite this: DOI: 10.1039/d3cp03844k

Prediction of superconductivity in metallic boron–carbon compounds from 0 to 100 GPa by high-throughput screening†

Feng Zheng,^{a,b} Yang Sun,^{b,*} Renhai Wang,^c Yimei Fang,^b Feng Zhang,^{de} Shunqing Wu,^{b,*} Qiubao Lin,^a Cai-Zhuang Wang,^{de} Vladimir Antropov^{de} and Kai-Ming Ho^d

Boron–carbon compounds have been shown to have feasible superconductivity. In our earlier paper [Zheng *et al.*, *Phys. Rev. B*, 2023, **107**, 014508], we identified a new conventional superconductor of LiB₃C at 100 GPa. Here, we aim to extend the investigation of possible superconductivity in this structural framework by replacing Li atoms with 27 different cations from periods 3, 4, and 5 under pressures ranging from 0 to 100 GPa. Using the high-throughput screening method of zone-center electron–phonon interaction, we found that ternary compounds like CaB₃C, SrB₃C, TiB₃C, and VB₃C are promising candidates for superconductivity. The consecutive calculations using the full Brillouin zone confirm that they have a T_c of <31 K at moderate pressures. Our study demonstrates that fast screening of superconductivity by calculating zone-center electron–phonon coupling strength is an effective strategy for high-throughput identification of new superconductors.

Received 11th August 2023,
Accepted 6th November 2023

DOI: 10.1039/d3cp03844k

rsc.li/pccp

1. Introduction

The search for novel materials with high-temperature or room-temperature superconductivity is currently one of the most active research fields in condensed matter physics. Extensive research has been conducted on H-rich compounds to explore possible high T_c superconductors inspired by Ashcroft's suggestion that pressurized hydrogen may become a high-temperature superconductor.¹ Thanks to key advances in the crystal structure search^{2–4} and first-principles calculations, several H-rich compounds are predicted to be promising conventional superconductors with high T_c (above 200 K) at high pressure (Megabar pressures).^{5–9} Experimental studies^{10–15} later confirmed the presence of superconductivity in some of these systems. Although these remarkable results suggest that

the conventional (electron–phonon) mechanism can achieve high T_c superconductivity, the high-pressure conditions required for these H-rich superconductors also limit their practical applications. Therefore, the focus of this field is gradually shifting towards finding new high- T_c materials that can operate at or close to ambient pressure.

Based on the Migdal–Eliashberg phonon-mediated theory, besides H-rich compounds, other light-element compounds such as boron or carbon compounds with strong covalent bonding and low phonon frequencies are also promising candidates for superconductors with high T_c .^{16–18} The current record for conventional superconductivity at ambient pressure is boron-doped Q-carbon with a T_c of 55 K.¹⁹ Another well-known superconductor is MgB₂ (39 K), with a layered metal-intercalated structure.¹⁶ Recently, a carbon–boron clathrate SrB₃C₃ was successfully synthesized at 57 GPa,²⁰ which can remain stable at atmospheric pressure and was theoretically predicted to be a superconductor with a T_c of ~40 K.^{21–23} This clathrate SrB₃C₃ composed of sp³ bonding represents a new class of carbon–boron superconductors with six four-sided and eight six-sided faces (4⁶6⁸). Using high-throughput density functional theory calculations on 105 XYB₆C₆ structures constructed by replacing Sr with two different metals in SrB₃C₃, Geng *et al.* proposed 18 new superconductors, and KPbB₆C₆ was predicted with an ambient-pressure T_c of 88 K.²⁴ In our previous paper, we also identified a new carbon–boron clathrate LiB₃C with eight four-sided faces and four six-sided faces

^a School of Science, Jimei University, Xiamen 361021, China.

E-mail: lqb@jmu.edu.cn

^b Department of Physics, OSED, Key Laboratory of Low Dimensional Condensed Matter Physics (Department of Education of Fujian Province), Juijiang Research Institute, Xiamen University, Xiamen 361005, China.

E-mail: yangsun@xmu.edu.cn, wsq@xmu.edu.cn

^c School of Physics and Optoelectronic Engineering, Guangdong University of Technology, Guangzhou 510006, China

^d Department of Physics, Iowa State University, Ames, Iowa 50011, USA

^e Ames Laboratory, U.S. Department of Energy, Ames, Iowa 50011, USA

† Electronic supplementary information (ESI) available. See DOI: <https://doi.org/10.1039/d3cp03844k>

(4^86^4) to be a conventional superconductor ($T_c \sim 22$ K) at 100 GPa.²⁵ Considering that element substitution in a prototype superconducting structure is a feasible strategy to obtain new superconductors, in this paper, we employed a high-throughput fast screening method of electron–phonon interaction to extend the investigation of possible superconductivity in the LiB₃C structure framework by replacing Li atoms with 27 different cations at 0, 25, 50, 75 and 100 GPa. This method is highly effective in screening candidates for superconductivity in large materials databases. Ternary compounds like CaB₃C, SrB₃C, TiB₃C, and VB₃C are found to be superconductors at moderate pressures.

2. Computational methods

First-principles calculations were performed by using the projector-augmented wave (PAW)²⁶ representations with density functional theory as implemented in the Vienna *ab initio* simulation package (VASP).^{27,28} The exchange and correlation energy was treated within the spin-polarized generalized gradient approximation (GGA) and parameterized by the Perdew–Burke–Ernzerhof (PBE) functional.²⁹ Wave functions were expanded in plane waves up to a kinetic energy cut-off of 520 eV. Brillouin-zone integrations were approximated using the special k -point sampling of the Monkhorst–Pack scheme³⁰ with a k -point mesh resolution of $2\pi \times 0.03 \text{ \AA}^{-1}$. Lattice vectors and atomic coordinates were fully relaxed until the force on each atom was less than 0.01 eV \AA^{-1} . The fast screening of electron–phonon coupling (EPC) constant λ_Γ at the Brillouin zone center was carried out based on the frozen-phonon method.³¹ The zone-center phonon was computed with the PHONOPY software,^{32,33} with a finer k -point sampling grid of $2\pi \times 0.02 \text{ \AA}^{-1}$ spacing and a criterion of a self-consistent calculation of 10^{-8} eV. The full Brillouin-zone EPC calculation was performed with the Quantum ESPRESSO (QE) code^{34,35} based on

the density-functional perturbation theory (DFPT).³⁶ Ultra-soft pseudopotentials from PSLibrary 1.0.0 (high accuracy)³⁷ for the PBE functional were used. The kinetic energy cut-offs were 75 Ry for wave functions and 576 Ry for potentials. The charge densities were determined on a k mesh of $20 \times 20 \times 20$. The dynamical matrices were calculated on a q mesh of $4 \times 4 \times 4$. The convergence threshold for self-consistency was 1×10^{-12} Ry. The Eliashberg spectral function and the EPC strength λ in the full Brillouin zone were calculated by using the electron–phonon linewidth. The superconducting T_c is determined using the Allen–Dynes (A–D) equation.³⁸ The effective screened Coulomb repulsion constant μ^* was 0.1 for the best-case scenario.

3. Results and discussion

3.1. Fast evaluation of the possible electron–phonon interactions of MB₃C (M = metal element)

The prototype structure LiB₃C was predicted to be a superconductor with a T_c of 22 K at 100 GPa, which has two PbO-type³⁹ layers of B₃C. Two B₃C layers are connected to form B–C cages with eight four-sided faces and four six-sided faces (4^86^4), as shown in Fig. 1(a). The cages are composed of 18 vertices with alternating C and B atoms, and each cage contains a single Li cation at the center. Since the light metal ions in boron–carbon compounds are more promising superconducting candidates,^{23,24} we substituted the Li site with 27 different metal ions M from periods 3, 4, and 5 (M = Na, Mg, Al, K, Ca, Sc, Ti, V, Cr, Mn, Fe, Co, Ni, Cu, Zn, Rb, Sr, Y, Zr, Nb, Mo, Tc, Ru, Rh, Pd, Ag, and Cd). Other metal ions from periods 6 and 7 with higher mass were not considered in this work. Each substituted structure and LiB₃C were relaxed by structural optimizations at 0, 25, 50, 75 and 100 GPa. These optimized structures were further analyzed by the high-throughput screening method with the zone-center EPC strength λ_Γ based on the frozen phonon method.³¹ As shown in Fig. 1(b), the

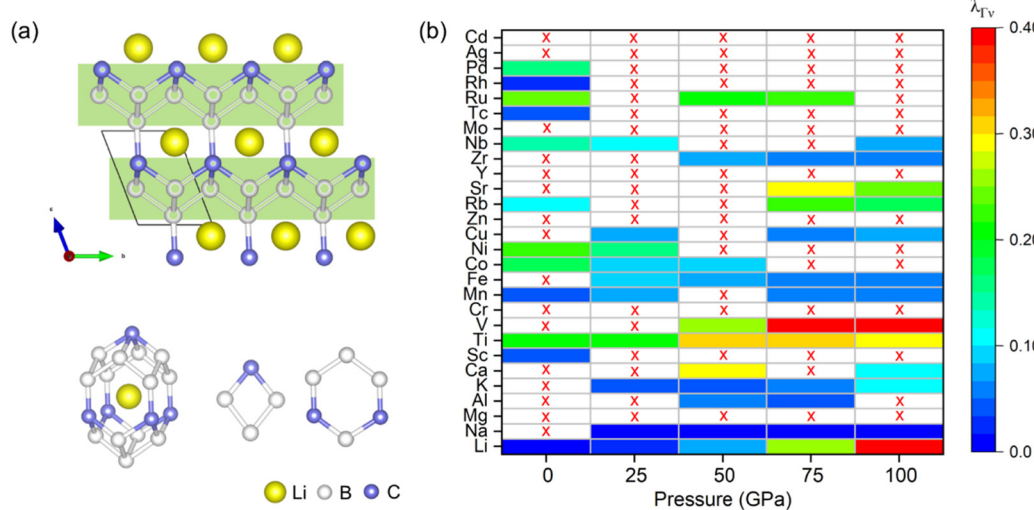


Fig. 1 (a) The prototype structure of LiB₃C. The light green rectangles denote PbO-type layers of B₃C. (b) The EPC constant λ_Γ at the Brillouin zone center of MB₃C structures at 0, 25, 50, 75, and 100 GPa.

dynamically unstable structures are marked with a cross, and dynamically stable phases are colored according to their λ_Γ (the summation of the zone-center EPC of all modes, *i.e.*, $\lambda_\Gamma = \sum_v \lambda_{\Gamma v}$). The reddish coding indicates stronger EPC. We use a sum $\sum_v \lambda_{\Gamma v} \sim 0.3$ threshold to screen out phases with suitable EPC. It can be found that LiB₃C has a high EPC at 100 GPa, which has been confirmed to be a superconductor by calculating EPC in the full Brillouin zone in our previous paper.²⁵ Besides LiB₃C at 100 GPa, we also identified four phases for further study, namely, CaB₃C (50 GPa), SrB₃C (75 GPa), TiB₃C (50, 75 and 100 GPa) and VB₃C (75 and 100 GPa).

3.2. Superconductivity and stability in CaB₃C, SrB₃C, TiB₃C and VB₃C

Because of the promising potential for superconductivity in CaB₃C (50 GPa), SrB₃C (75 GPa), TiB₃C (50, 75, and 100 GPa), and VB₃C (75 and 100 GPa), we perform DFPT calculations to compute their full Brillouin zone EPC constant and calculate T_c using the A-D equation.

CaB₃C. Fig. 2(a) shows the phonon linewidth (γ_{qv})-weighted phonon spectrum, projected phonon density of states (PHDOS), and Eliashberg spectral function $\alpha^2 F(\omega)$ of CaB₃C at 50 GPa. It can be found that acoustic modes have a sizable phonon linewidth, which are mainly attributed to the vibrations of Ca atoms, as indicated by the PHDOS. Furthermore, one can see that phonon modes 4, 5, 9, 12, and 13 also have a large contribution to the phonon linewidth and correspondingly to the electron–phonon interaction at the Γ point, which agrees well with the fast-screening results as shown in Fig. S1(a) (ESI†). Modes 9 and 12 show a large phonon linewidth along $(1/4)Y-\Gamma-A-(1/3)L_2$. The vibrational configurations of these modes at the Γ point are shown in Fig. S5 (ESI†). Mode 9 corresponds to stretching vibrations of B2 and B3 atoms, and mode 12 undergoes a stretching vibration of C and B1 atoms, which are all along the *c* axis. The integrated EPC parameter λ of CaB₃C at 50 GPa is 1.69. The ω_{\log} value can be obtained from the A–D equation at 237.6 K, and we predict $T_c = 31$ K ($\mu^* = 0.1$). As a comparison, we also compute the EPC for the CaB₃C at 100 GPa, as shown in Fig. 2(b), which is not expected to show

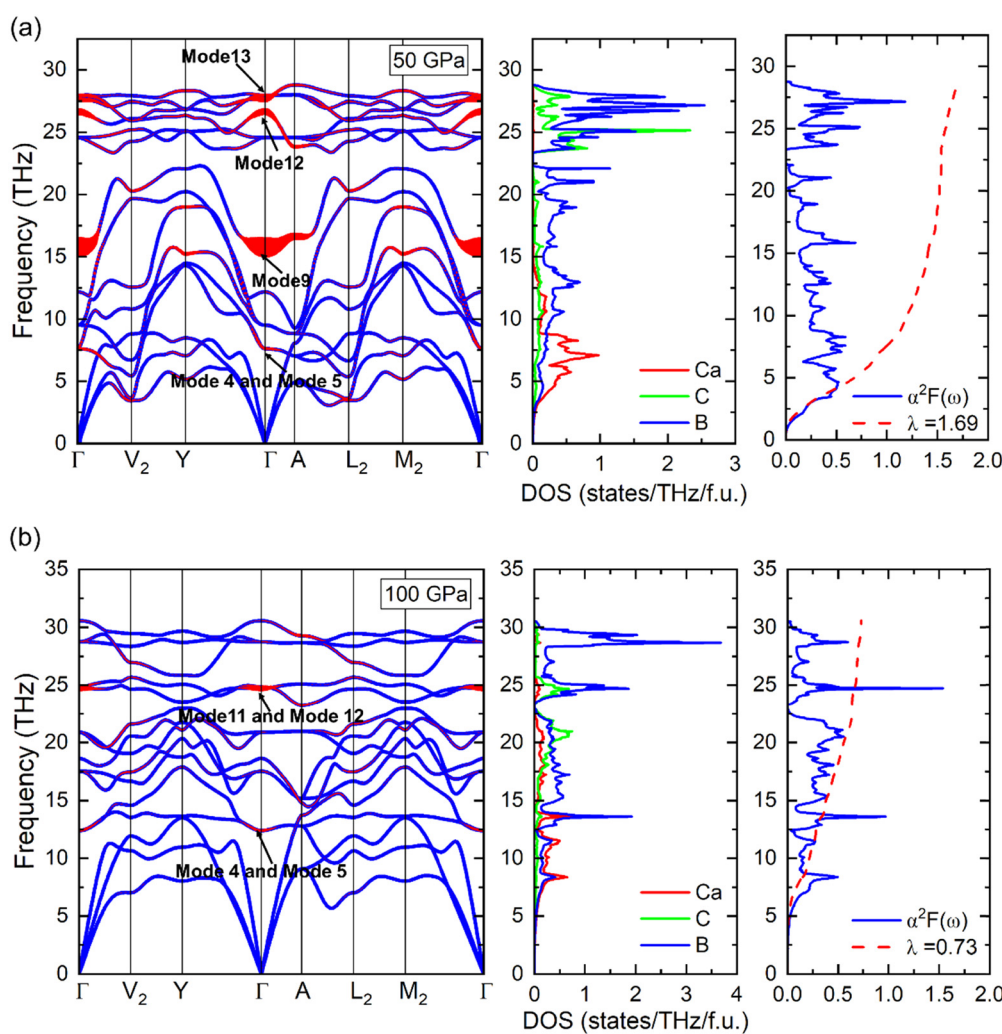


Fig. 2 The γ_{qv} -weighted phonon spectrum, projected phonon density of states (PHDOS) and Eliashberg spectral function $\alpha^2 F(\omega)$ of CaB₃C at (a) 50 and (b) 100 GPa.

a strong EPC from the zone-center EPC calculation. The integrated EPC parameter λ is 0.73 for CaB_3C at 100 GPa. It can be observed that the large phonon linewidth of acoustic modes disappears in CaB_3C at 100 GPa. Moreover, only phonon modes 4, 5, 11, and 12 contribute to the phonon linewidth at the Γ point. This also aligns with the fast-screening results, as shown in Fig. S1(b) (ESI†). The vibrational configurations of these modes at the Γ point are shown in Fig. S6 (ESI†), and one can see that the vibrations of mode 11 at 100 GPa are identical to those of mode 9 at 50 GPa (Fig. S5, ESI†). Both correspond to stretching vibrations of B_2 and B_3 atoms along the c -axis. This indicates that the original phonon mode 9 undergoes hardening as pressures increase from 50 to 100 GPa of CaB_3C . The difference in λ between CaB_3C at 50 and 100 GPa can be explained by their distinct density of states (DOS) at the Fermi level (E_f). As shown in Fig. 3(a and b), the electronic properties of CaB_3C exhibit metallic features with DOS crossing the E_f at 50 and 100 GPa. The calculated total DOS at the E_f is 1.17 and 0.70 eV⁻¹ per f.u. at 50 and 100 GPa, respectively. Such a difference in the total DOS at the E_f can be attributed to the difference in structural features of CaB_3C at 50 and 100 GPa. As shown in Fig. 3(d), at 50 GPa, two PbO-type layers of B_3C (marked with light green rectangles) in CaB_3C are separated by 3.08 Å due to low pressure. The $\text{B}1$ and $\text{C}1$ atoms cannot connect to form a bond, which leads to high DOS at the E_f

(Fig. 3(c)). However, at 100 GPa (Fig. 3(e)), boron and carbon in CaB_3C can retain the prototype structure of LiB_3C , which forms a clathrate structure, and two layers of B_3C relate to $\text{B}1$ and $\text{C}1$ atoms to form a strong B–C bond (~1.95 Å). This leads to the DOS of $\text{B}1$ and $\text{C}1$ atoms moving towards a lower energy level (Fig. 3(c)). We also calculated the electron localization function (ELF) and crystal orbital Hamilton population (COHP)⁴⁰ to further explore the chemical bonds between $\text{B}1$ and $\text{C}1$. As shown in Fig. S9(a) and (b) (ESI†), at 50 GPa, there is no electron localization between $\text{B}1$ and $\text{C}1$, which suggests that they do not form a B–C bond. While, for CaB_3C at 100 GPa, the value of ELF is ~0.75 between $\text{B}1$ and $\text{C}1$, which indicates that they form covalent bonding. The COHP also indicates the same trend. As shown in Fig. S10 (ESI†), the negative COHP indicates bonding, and the positive COHP indicates antibonding. One can observe a different picture of $\text{B}1$ – $\text{C}1$ bonding where CaB_3C at 100 GPa has a stronger $\text{B}1$ – $\text{C}1$ bond than that of CaB_3C at 50 GPa. Therefore, the significant difference of DOS at the E_f between CaB_3C at 50 and 100 GPa can be attributed to the different characteristics of chemical bonds between $\text{B}1$ and $\text{C}1$, which leads to their difference in λ . While due to a larger average phonon frequency ($\omega_{\log} \sim 651.3$ K), the T_c of CaB_3C at 100 GPa can also reach up to 25 K. The superconducting parameters of CaB_3C at 50 and 100 GPa are summarized in Fig. 3(f).

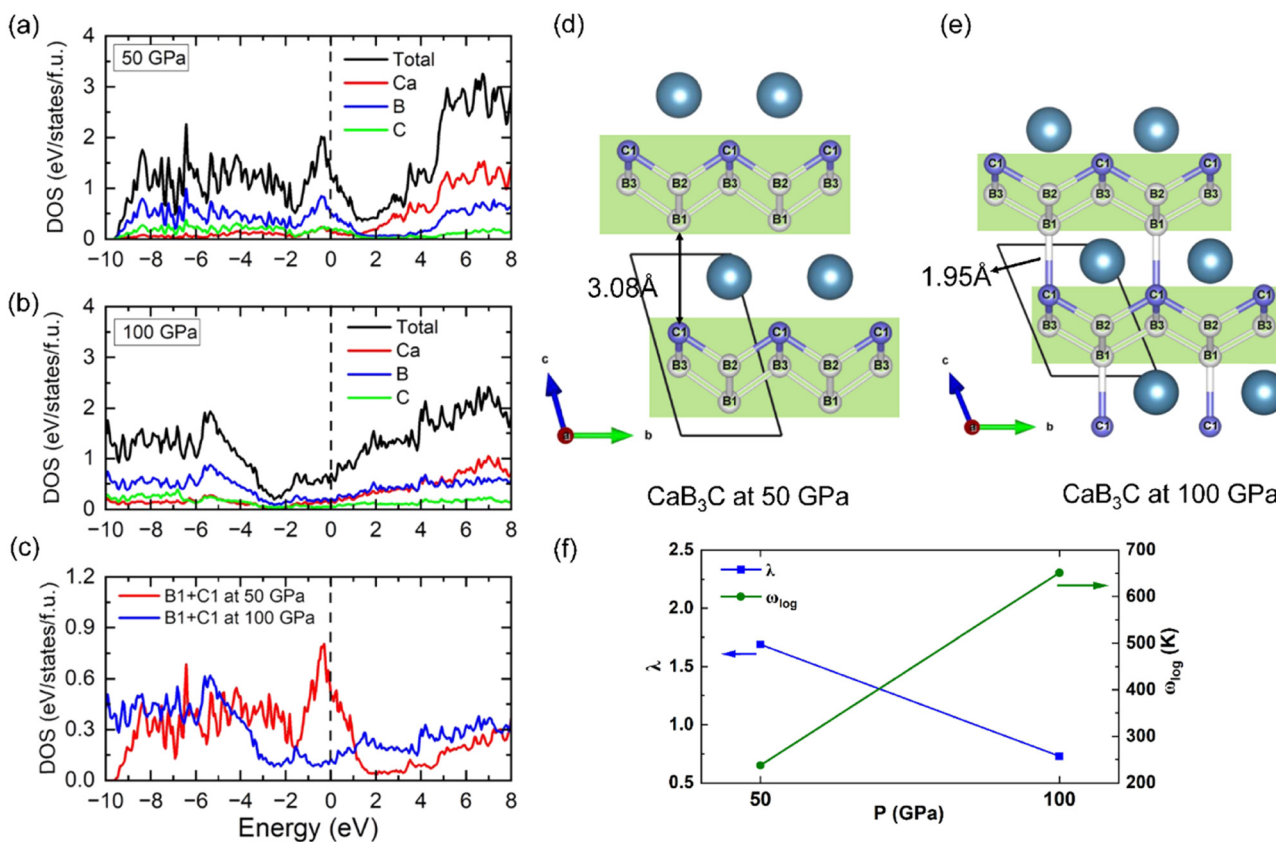


Fig. 3 The electronic density of states (DOS) of CaB_3C at (a) 50 and (b) 100 GPa. (c) The projected DOS of $\text{B}1$ and $\text{C}1$ atoms at 50 and 100 GPa. The crystal structure of CaB_3C at (d) 50 and (e) 100 GPa. The light green rectangles denote PbO-type layers of B_3C . (f) The calculated superconducting parameters of CaB_3C at 50 and 100 GPa.

SrB₃C. Fig. 4(a) shows the calculated γ_{qv} -weighted phonon dispersion and PHDOS of SrB₃C at 75 GPa, together with the Eliashberg spectral function $\alpha^2F(\omega)$. It can be found that the phonon dispersion can be separated into two regions: the lower

frequency modes (typically below 7.5 THz) are mainly associated with Sr atoms, and the higher frequency modes can be attributed to boron and carbon atoms. In addition, phonon modes 4, 5, 9, 12, 13, and 14 significantly contribute to the

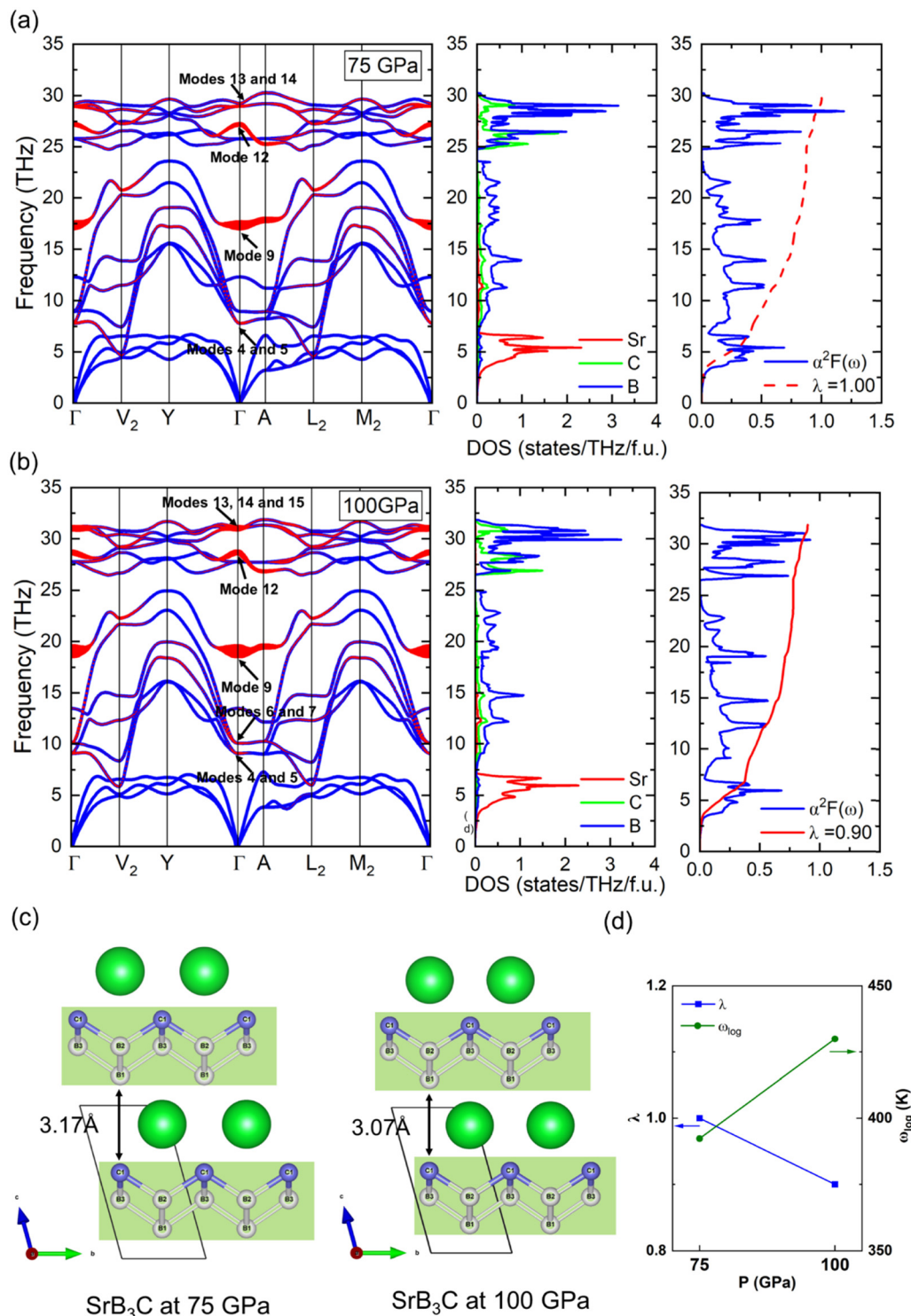


Fig. 4 The γ_{qv} -weighted phonon spectrum, projected phonon density of states (PHDOS), and Eliashberg spectral function $\alpha^2F(\omega)$ of SrB₃C at (a) 75 and (b) 100 GPa. (c) Crystal structures of SrB₃C at 75 and 100 GPa. The light green rectangles denote PbO-type layers of B₃C. (d) The calculated superconducting parameters of SrB₃C at 75 and 100 GPa.

phonon linewidth at the near Γ point. The vibrational configurations of these modes at the Γ point are shown in Fig. S7 (ESI†), which all involve boron and carbon atom vibrations. Like CaB_3C at 50 GPa, SrB_3C at 75 GPa exhibits a large phonon linewidth along the $(1/4)\text{Y}-\Gamma-\text{A}-(1/3)L_2$ of phonon modes 9 and 12. However, the values of the phonon linewidth are smaller than those of CaB_3C at 50 GPa and their frequencies are higher than those of CaB_3C at 50 GPa. This leads to a lower total λ of SrB_3C at 75 GPa. Our calculated total λ is 1.00, and the ω_{\log} value is 392.3 K. We estimated $T_c = 27$ K with $\mu^* = 0.1$ by solving the A-D equation. The crystal structure of SrB_3C at 75 GPa is shown in Fig. 4(c), which is similar to that of CaB_3C at 50 GPa. The distance between the two layers of B_3C is 3.17 Å. Unlike CaB_3C at 100 GPa, SrB_3C still has two layers of B_3C separated even at 100 GPa (3.07 Å), which can be attributed to its larger ionic radius than that of Ca as listed in Table S1 (ESI†) (In the LiB_3C prototype structure, Ca and Sr are coordinated to four C's and four B's as shown in Fig. S13 (ESI†)). Based on the basic physical properties of Ca and Sr in this link,⁴¹ the ionic radii of Ca and Sr in 8-coordinate are 1.26 and 1.40 Å, respectively). The calculated ELF (Fig. S9 (c) and (d), ESI†) and COHP (Fig. S11, ESI†) suggest that the two layers of B_3C of SrB_3C at 75 and 100 GPa do not form a B–C bond. Due to the similar structure, the phonon spectrum of SrB_3C at 100 GPa (Fig. 4(b)) is barely

distinguishable from that of 75 GPa (Fig. 4(a)). It can be found that phonon modes 4, 5, 6, 7, 9, 12, 13, 14, and 15 greatly contribute to the phonon linewidth at the near Γ point. The vibrational configurations of these modes at the Γ point are seen in Fig. S8 (ESI†), which all involve boron and carbon atom vibrations. The integrated EPC parameter λ of SrB_3C at 100 GPa is 0.90, slightly lower than that of 75 GPa. The ω_{\log} value of SrB_3C at 100 GPa is 429.2 K, and the T_c is 24 K. The superconducting parameters of SrB_3C at 75 and 100 GPa are summarized in Fig. 4(d).

TiB₃C and VB₃C. Fig. 5(a) shows the γ_{qv} -weighted phonon spectrum, PHDOS, Eliashberg spectral function $\alpha^2F(\omega)$, and the crystal structure of TiB_3C at 50 GPa. Because of the shift of boron chains, TiB_3C forms an irregular B–C structural framework at 50 GPa. The EPC is primarily derived from phonon modes at the zone center of TiB_3C at 50 GPa. Our calculated integrated EPC parameter λ is 0.80. We obtain the ω_{\log} value of 507.2 K and predict $T_c = 24$ K for TiB_3C at 50 GPa. The corresponding superconductivity properties of TiB_3C at 75 and 100 GPa are shown in Fig. S14 (ESI†). When pressures are up to 75 and 100 GPa, it can be observed that the λ value of TiB_3C is slightly decreased. The calculated T_c of TiB_3C are 23 and 21 K at 75 and 100 GPa, respectively. The structural feature of VB_3C is similar to that of TiB_3C , which also cannot retain PbO-type B–C

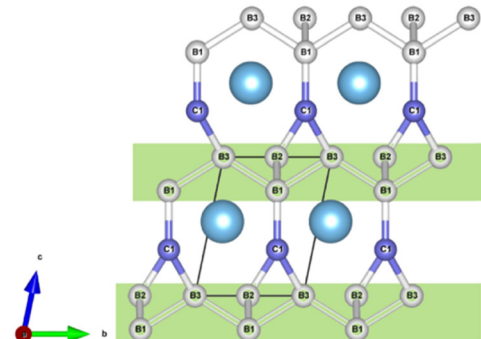
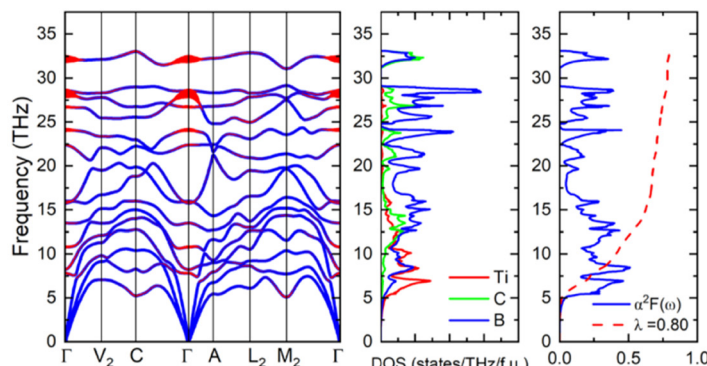
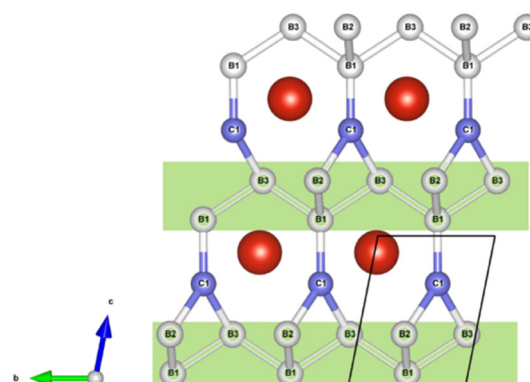
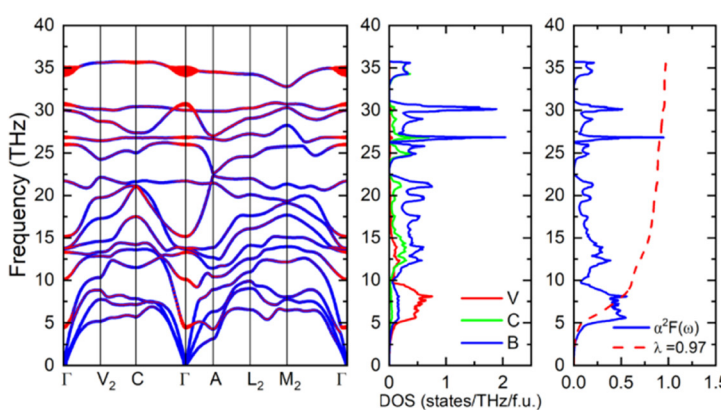
(a) TiB₃C at 50 GPa(b) VB₃C at 75 GPa

Fig. 5 The γ_{qv} -weighted phonon spectrum, projected phonon density of states (PHDOS), Eliashberg spectral function $\alpha^2F(\omega)$, and crystal structure of (a) TiB_3C at 50 GPa and (b) VB_3C at 75 GPa. The light green rectangles denote the shift of boron chains.

Table 1 The enthalpy above the convex hull (H_d) (eV per atom) of ternary CaB_3C , SrB_3C , TiB_3C , and VB_3C compounds at a given pressure

	CaB_3C	SrB_3C	TiB_3C	VB_3C
50 GPa	0.252	0.259	0.568	0.633
75 GPa	0.306	0.356	0.539	0.615
100 GPa	0.260	0.31	0.521	0.604

layers, as shown in Fig. 5(b). The shifted boron chains connect with B1 and C1 atoms. The calculated ELF (Fig. S9(e) and (f), ESI†) and COHP (Fig. S12, ESI†) indicate that B1 and C1 form covalent bonding in TiB_3C at 50 GPa and VB_3C at 75 GPa. The integrated EPC parameter λ of VB_3C is 0.97 at 75 GPa, and the T_c is 29 K. At 100 GPa, the λ value of VB_3C is 0.88, as shown in Fig. S15 (ESI†), and we predicted its T_c of 26 K.

We plotted the pressure dependence of the T_c of CaB_3C , SrB_3C , TiB_3C , and VB_3C compounds as shown in Fig. S16 (ESI†), which suggests the decrease of T_c with the increase of pressure. For the CaB_3C compound, with the increased pressure (at 100 GPa), B1 and C1 connect to form a strong bond (Fig. 3(e)), which results in a reduced density of states (DOS) at E_f (Fig. 3(c)) and lowers the T_c . For the SrB_3C , TiB_3C , and VB_3C compounds, their crystal structures remain unchanged under increasing pressures, resulting in phonon spectra that are difficult to distinguish (Fig. 4(a), (b), Fig. 5 and Fig. S14, S15, ESI†). The pressure only causes phonon modes to harden, which lowers the electron–phonon coupling strength (λ) and reduces their T_c .

Since the CaB_3C , SrB_3C , TiB_3C , and VB_3C compounds have been confirmed to be superconductors by full Brillouin zone EPC calculations, it is necessary to further investigate their thermodynamic stability. We calculate their relative stability under the corresponding pressure, depending on the calculated formation enthalpies $H_f = \frac{H(\text{XB}_3\text{C}) - H(\text{X}) - 3H(\text{B}) - H(\text{C})}{5}$, where $H(\text{XB}_3\text{C})$ is the total enthalpy of the XB_3C compound at a given pressure, and $H(\text{X})$, $H(\text{B})$, and $H(\text{C})$ are the enthalpy of the three elements in their ground-state structure at the same pressure. Also, H_d is introduced as the enthalpy above the convex hull to represent the relative stability on the phase diagram. Ground-state phases have $H_d = 0$. As shown in Table 1, these compounds all have positive H_d , which indicates that they are all metastable. Furthermore, CaB_3C and SrB_3C have lower H_d than those of TiB_3C and VB_3C . These results suggest that crystal structures that can retain PbO-type B_3C layered structures show better thermodynamic stability. Especially, for CaB_3C at 50 and 100 GPa, their H_d values are close to 0.25 eV per atom, which indicates that they may be realized under appropriate experimental conditions.

4. Conclusions

Using a high-throughput screening method, we performed a broad-range study of the superconductivity of metal-substituted LiB_3C . The prototype structure LiB_3C was predicted to be a superconductor in our previous paper, which has two PbO-type

layers of B_3C and two B_3C layers connected to form a B–C clathrate structure. Ternary compounds like CaB_3C , SrB_3C , TiB_3C , and VB_3C are found to be superconductors at moderate pressures. CaB_3C can retain the B–C clathrate structure at 100 GPa and has superconductivity with an EPC constant of $\lambda = 0.73$ and a T_c of 25 K. However, at 50 GPa, two PbO-type B_3C layers in CaB_3C are separated by a distance due to low pressure, which leads to higher DOS at the E_f than that at 100 GPa. Therefore, CaB_3C has a higher EPC constant λ of 1.69 and a $T_c = 31$ K at 50 GPa. For SrB_3C , due to the larger ionic radius of Sr, two PbO-type B_3C layers are always separated at 75 and 100 GPa. The calculated results show that SrB_3C has T_c of 27 K and 24 K at 75 and 100 GPa, respectively. Because of the B chain shift, TiB_3C and VB_3C cannot retain PbO-type B_3C layers and form an irregular B–C structural framework. The EPC constant λ is 0.80, and the T_c is 24 K for TiB_3C at 50 GPa and is slightly decreased with pressures up to 75 and 100 GPa. VB_3C has a EPC constant λ of 0.97 and a T_c of 29 K at 75 GPa, which also slightly decreases when the pressure is up to 100 GPa. The demonstrated consistency between the zone-center electron–phonon interaction calculations and DFPT exploration validates this high-throughput screening approach. This strategy allows a much faster screening process, making it a powerful tool for accelerating the discovery of new functional materials.

Conflicts of interest

There are no conflicts to declare.

Acknowledgements

F. Zheng was supported by the Research Foundation of Jimei University (ZQ2023013). Work at Xiamen University was supported by the National Natural Science Foundation of China (11874307). Y. S. acknowledges the support of the Natural Science Foundation of Xiamen, China (Grant No. 3502Z202371007) and the Fundamental Research Funds for the Central Universities (20720230014). R. W. was supported by the Guangdong Basic and Applied Basic Research Foundation (Grant No. 2021A1515110328 and 2022A1515012174). V. A., C. Z. Wang, and F. Zhang were supported by the U.S. Department of Energy (DOE), Office of Science, Basic Energy Sciences, Materials Science and Engineering Division. Ames Laboratory is operated for the U.S. DOE by the Iowa State University under Contract No. DE-AC02-07CH11358, including the grant of computer time at the National Energy Research Supercomputing Center (NERSC) in Berkeley. S. Fang and T. Wu from the Information and Network Center of Xiamen University are acknowledged for the help with GPU computing.

References

- 1 N. W. Ashcroft, *Phys. Rev. Lett.*, 1968, **21**, 1748–1749.
- 2 J. Wang, H. Gao, Y. Han, C. Ding, S. Pan and Y. Wang, *et al.*, *Natl. Sci. Rev.*, 2023, **10**, nwad128.

- 3 S. Q. Wu, M. Ji, C. Z. Wang, M. C. Nguyen, X. Zhao, K. Umemoto, R. M. Wentzcovitch and K. M. Ho, *J. Phys.: Condens. Matter*, 2014, **26**, 035402.
- 4 Y. Wang, J. Lv, L. Zhu and Y. Ma, *Comput. Phys. Commun.*, 2012, **183**, 2063–2070.
- 5 D. Duan, Y. Liu, F. Tian, D. Li, X. Huang and Z. Zhao, *et al.*, *Sci. Rep.*, 2014, **4**, 6968.
- 6 F. Peng, Y. Sun, C. J. Pickard, R. J. Needs, Q. Wu and Y. Ma, *Phys. Rev. Lett.*, 2017, **119**, 107001.
- 7 H. Liu, I. I. Naumov, R. Hoffmann, N. W. Ashcroft and R. J. Hemley, *Proc. Natl. Acad. Sci. U. S. A.*, 2017, **114**, 6990–6995.
- 8 H. Wang, J. S. Tse, K. Tanaka, T. Iitaka and Y. M. Ma, *Proc. Natl. Acad. Sci. U. S. A.*, 2012, **109**, 6463–6466.
- 9 H. Xie, Y. Yao, X. Feng, D. Duan, H. Song and Z. Zhang, *et al.*, *Phys. Rev. Lett.*, 2020, **125**, 217001.
- 10 A. P. Drozdov, M. I. Eremets, I. A. Troyan, V. Ksenofontov and S. I. Shylin, *Nature*, 2015, **525**, 73–76.
- 11 P. Kong, V. S. Minkov, M. A. Kuzovnikov, A. P. Drozdov, S. P. Besedin and S. Mozaffari, *et al.*, *Nat. Commun.*, 2021, **12**, 5075.
- 12 E. Snider, N. Dasenbrock-Gammon, R. McBride, X. Wang, N. Meyers, K. V. Lawler, E. Zurek, A. Salamat and R. P. Dias, *Phys. Rev. Lett.*, 2021, **126**, 117003.
- 13 M. Somayazulu, M. Ahart, A. K. Mishra, Z. M. Geballe, M. Baldini, Y. Meng, V. V. Struzhkin and R. J. Hemley, *Phys. Rev. Lett.*, 2019, **122**, 027001.
- 14 A. P. Drozdov, P. P. Kong, V. S. Minkov, S. P. Besedin, M. A. Kuzovnikov and S. Mozaffari, *et al.*, *Nature*, 2019, **569**, 528–531.
- 15 L. Ma, K. Wang, Y. Xie, X. Yang, Y. Wang and M. Zhou, *et al.*, *Phys. Rev. Lett.*, 2022, **128**, 167001.
- 16 J. Nagamatsu, N. Nakagawa, T. Muranaka, Y. Zenitani and J. Akimitsu, *Nature*, 2001, **410**, 63–64.
- 17 J. M. An and W. E. Pickett, *Phys. Rev. Lett.*, 2001, **86**, 4366–4369.
- 18 L. Boeri, J. Kortus and O. K. Andersen, *Phys. Rev. Lett.*, 2004, **93**, 237002.
- 19 A. Bhaumik, R. Sachan, S. Gupta and J. Narayan, *ACS Nano*, 2017, **11**, 11915–11922.
- 20 L. Zhu, G. M. Borstad, H. Y. Liu, P. A. Gunka, M. Guerette and J. A. Dolyniuk, *et al.*, *Sci. Adv.*, 2020, **6**, eaay8361.
- 21 J.-N. Wang, X.-W. Yan and M. Gao, *Phys. Rev. B*, 2021, **103**, 144515.
- 22 L. Zhu, H. Liu, M. Somayazulu, Y. Meng, P. A. Guńka and T. B. Shiell, *et al.*, *Phys. Rev. Res.*, 2023, **5**, 013012.
- 23 S. Di Cataldo, S. Qulaghasi, G. B. Bachelet and L. Boeri, *Phys. Rev. B*, 2022, **105**, 064516.
- 24 N. S. Geng, K. P. Hilleke, L. Zhu, X. Y. Wang, T. A. Strobel and E. Zurek, *J. Am. Chem. Soc.*, 2023, **143**, 1696–1706.
- 25 F. Zheng, Y. Sun, R. H. Wang, Y. M. Fang, F. Zhang, S. Q. Wu, C. Z. Wang, V. Antropov and K. M. Ho, *Phys. Rev. B*, 2023, **107**, 014508.
- 26 G. Kresse and D. Joubert, *Phys. Rev. B: Condens. Matter Mater. Phys.*, 1999, **59**, 1758–1775.
- 27 G. Kresse and J. Furthmüller, *Phys. Rev. B: Condens. Matter Mater. Phys.*, 1996, **54**, 11169–11186.
- 28 G. Kresse and J. Furthmüller, *Comput. Mater. Sci.*, 1996, **6**, 15–50.
- 29 J. P. Perdew, K. Burke and M. Ernzerhof, *Phys. Rev. Lett.*, 1996, **77**, 3865–3868.
- 30 H. J. Monkhorst and J. D. Pack, *Phys. Rev. B: Solid State*, 1976, **13**, 5188–5192.
- 31 Y. Sun, F. Zhang, C. Z. Wang, K. M. Ho, I. I. Mazin and V. Antropov, *Phys. Rev. Mater.*, 2022, **6**, 074801.
- 32 A. Togo, F. Oba and I. Tanaka, *Phys. Rev. B: Condens. Matter Mater. Phys.*, 2008, **78**, 134106.
- 33 A. Togo and I. Tanaka, *Scr. Mater.*, 2015, **108**, 1–5.
- 34 P. Giannozzi, S. Baroni, N. Bonini, M. Calandra, R. Car and C. Cavazzoni, *et al.*, *J. Phys.: Condens. Matter*, 2009, **21**, 395502.
- 35 P. Giannozzi, O. Andreussi, T. Brumme, O. Bunau, M. B. Nardelli and M. Calandra, *et al.*, *J. Phys.: Condens. Matter*, 2017, **29**, 465901.
- 36 S. Baroni, S. de Gironcoli, A. Dal Corso and P. Giannozzi, *Rev. Mod. Phys.*, 2001, **73**, 515–562.
- 37 A. Dal Corso, *Comput. Mater. Sci.*, 2014, **95**, 337–350.
- 38 P. B. Allen and R. C. Dynes, *Phys. Rev. B: Solid State*, 1975, **12**, 905–922.
- 39 D. E. Bugaris, M. Sturza, F. Han, J. Im, D. Y. Chung, A. J. Freeman and M. G. Kanatzidis, *Eur. J. Inorg. Chem.*, 2015, 2164–2172.
- 40 R. Dronskowski and P. E. Blochl, *J. Phys. Chem.*, 1993, **97**, 8617–8624.
- 41 <https://webelements.com>.

Supplemental Materials

Prediction of superconductivity in metallic boron-carbon compounds from 0 to 100 GPa by high-throughput screening

Feng Zheng^{1,2}, Yang Sun^{2*}, Renhai Wang³, Yimei Fang², Feng Zhang^{4,5}, Shunqing Wu^{2*}, Qiubao Lin^{1*}, Cai-Zhuang Wang^{4,5}, Vladimir Antropov^{4,5}, Kai-Ming Ho⁴

¹School of Science, Jimei University, Xiamen 361021, China

²Department of Physics, OSED, Key Laboratory of Low Dimensional Condensed Matter Physics (Department of Education of Fujian Province), Jiujiang Research Institute, Xiamen University, Xiamen 361005, China.

³School of Physics and Optoelectronic Engineering, Guangdong University of Technology, Guangzhou 510006, China

⁴Department of Physics, Iowa State University, Ames, Iowa 50011, United States

⁵Ames Laboratory, U.S. Department of Energy, Ames, Iowa 50011, USA

SUPPLEMENTARY MATERIALS

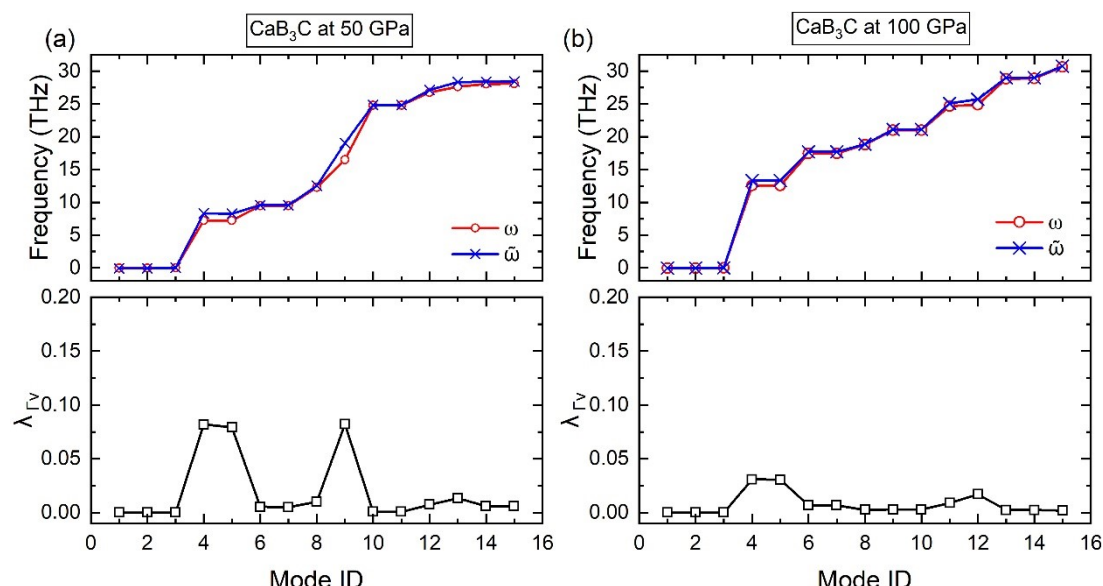


Fig. S1. The screened and unscreened phonon frequency (top panel) and zone-center EPC strength (bottom panel) in CaB₃C at (a) 50 and (b) 100 GPa.

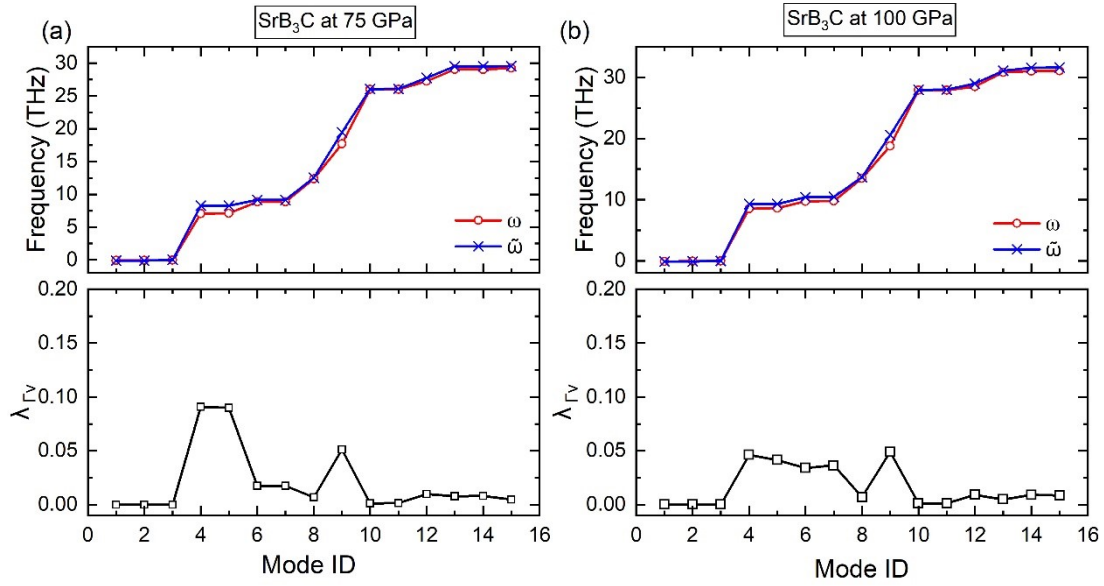


Fig. S2. The screened and unscreened phonon frequency (top panel) and zone-center EPC strength (bottom panel) in SrB_3C at (a) 50 and (b) 100 GPa.

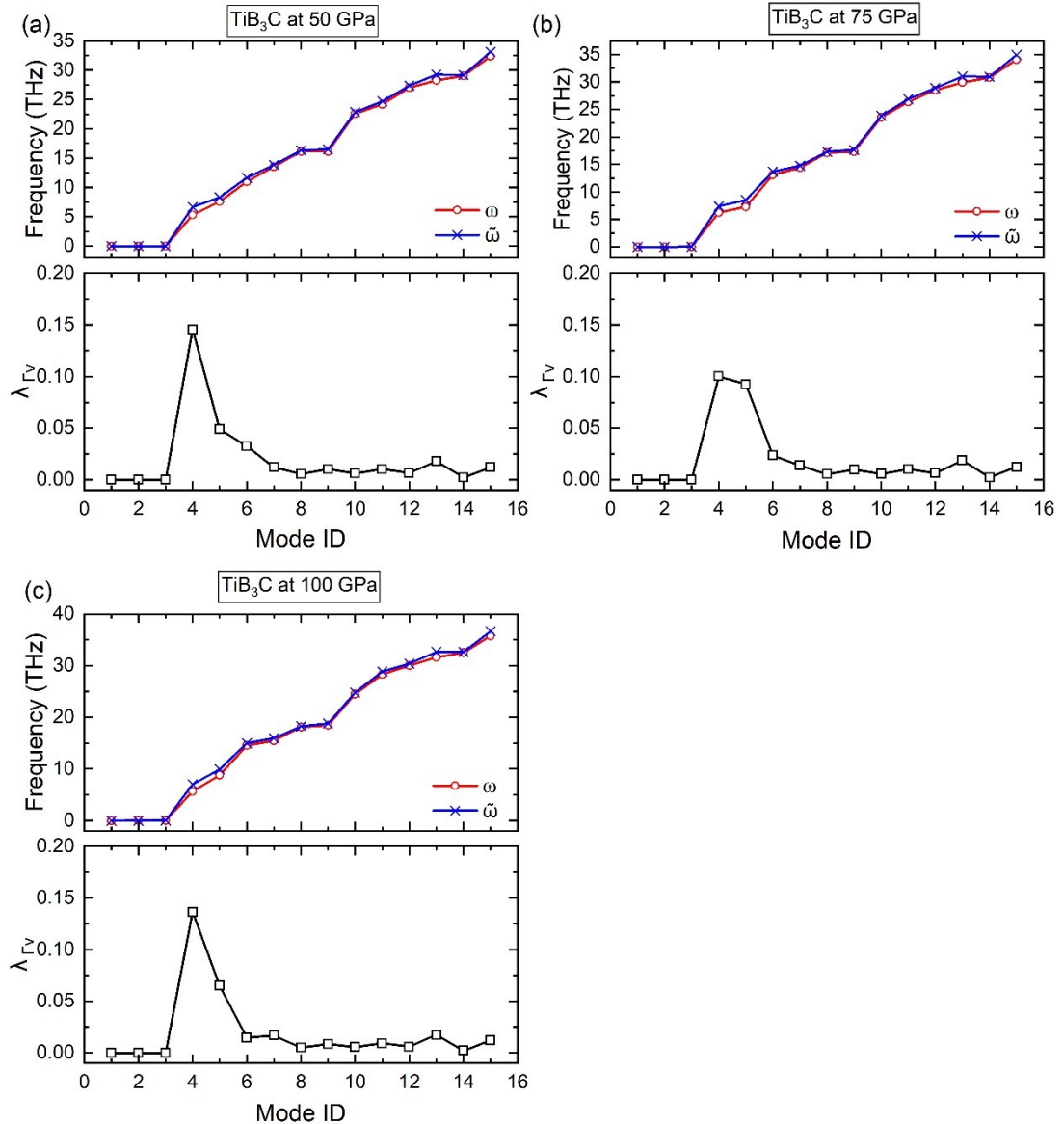


Fig. S3. The screened and unscreened phonon frequency (top panel) and zone-center EPC strength (bottom panel) in TiB_3C at (a) 50, (b) 75 and (c) 100 GPa.

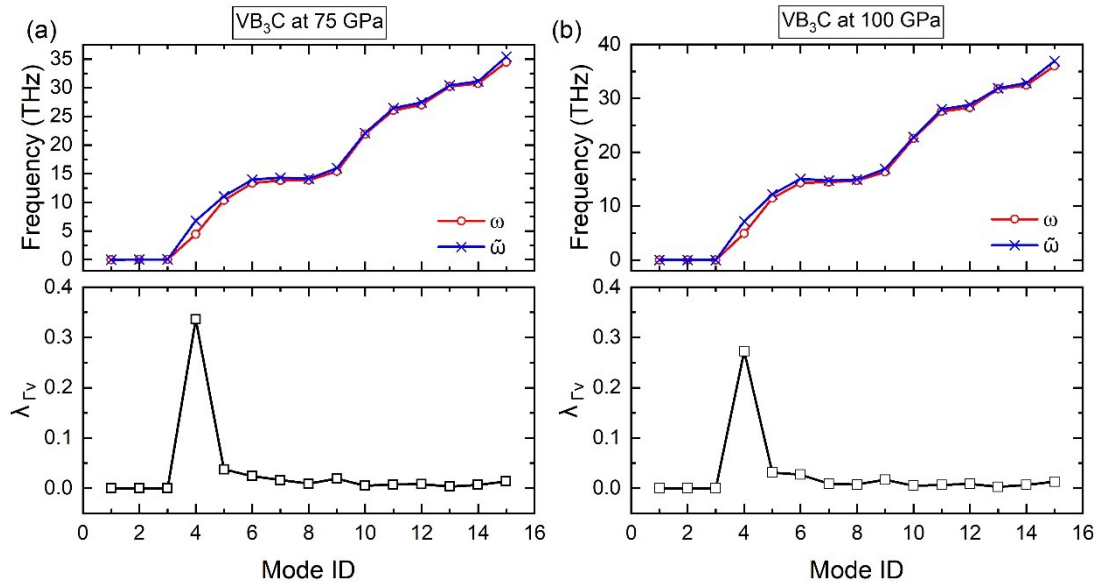


Fig. S4. The screened and unscreened phonon frequency (top panel) and zone-center EPC strength (bottom panel) in VB_3C at (a) 75 and (b) 100 GPa.

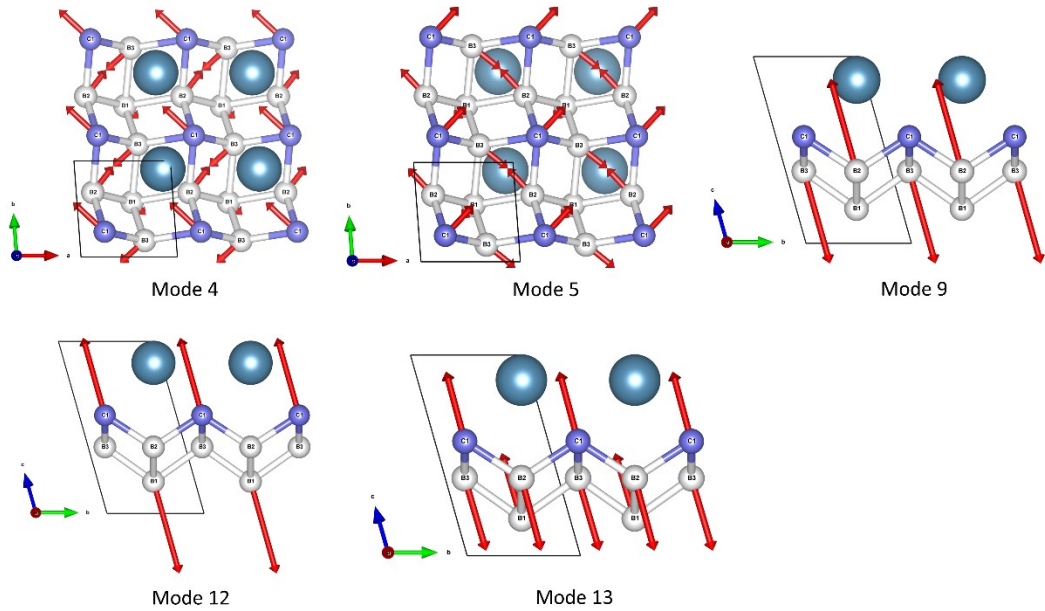


Fig. S5. The vibrational patterns for modes 4, 5, 9, 12, and 13 at the Γ point of CaB_3C at 50 GPa.

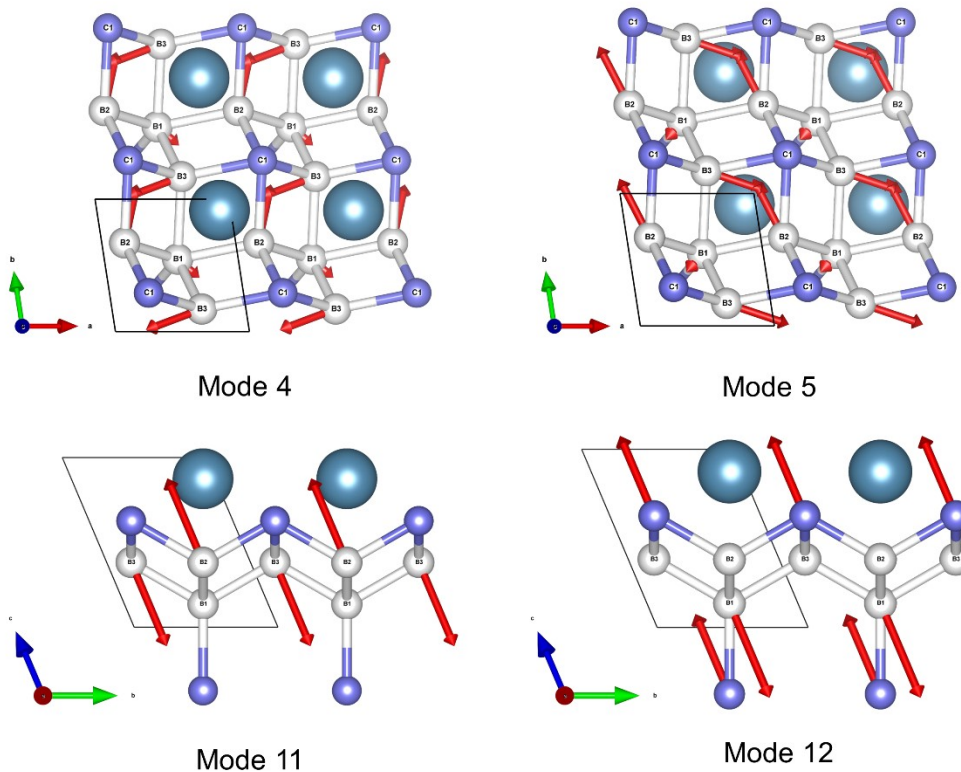


Fig. S6. The vibrational patterns for modes 4, 5, 11, and 12 at the Γ point of CaB_3C at 100 GPa.

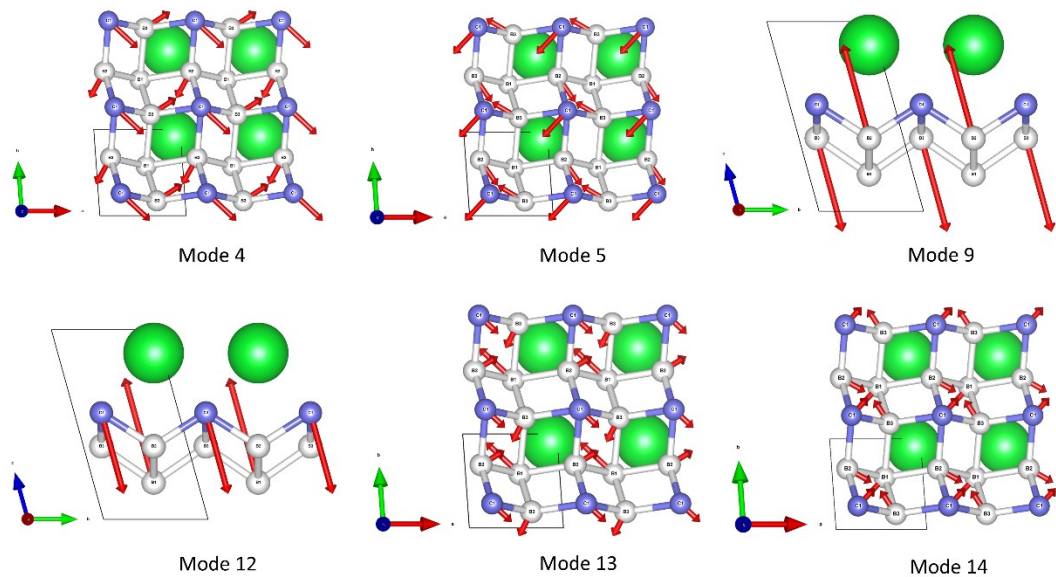


Fig. S7. The vibrational patterns for modes 4, 5, 9, 12, 13, and 14 at the Γ point of SrB_3C at 75 GPa

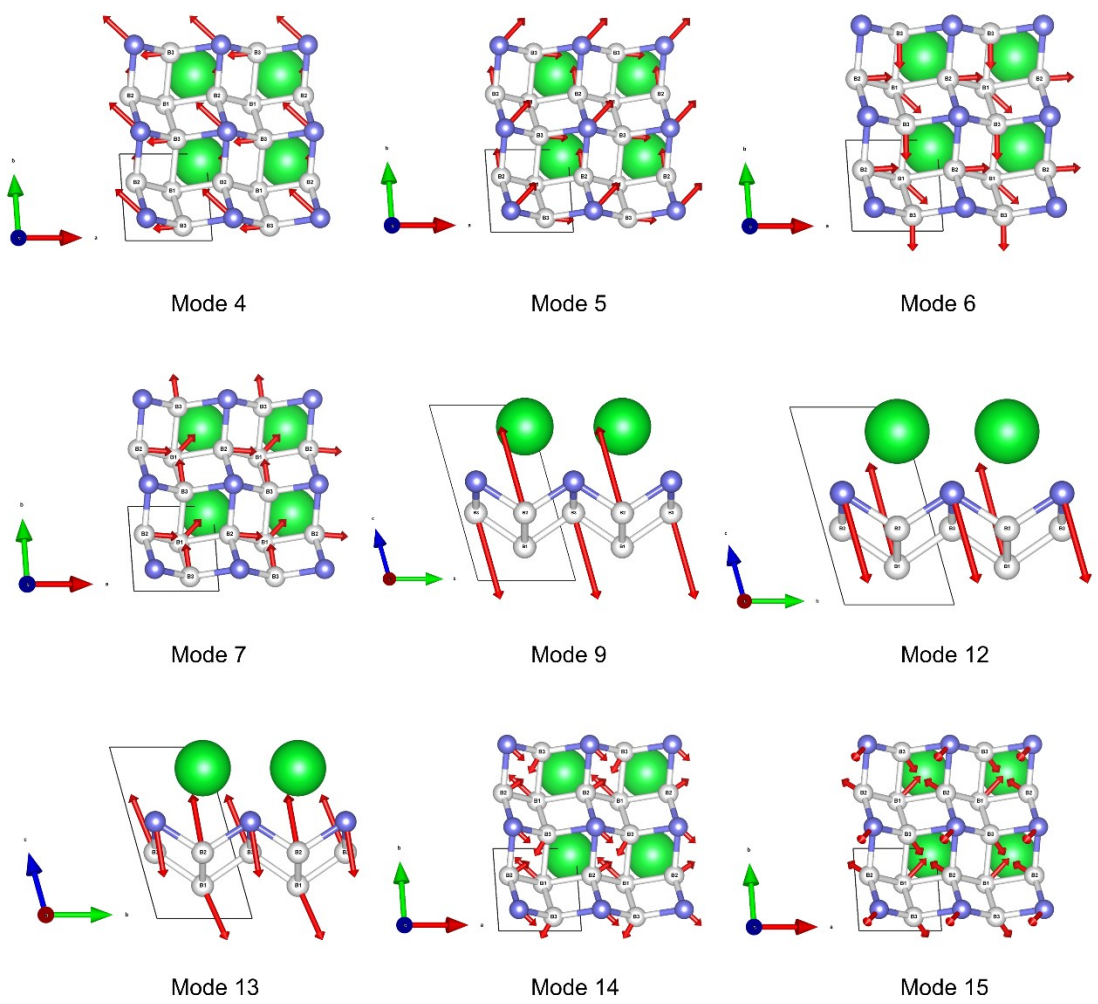


Fig. S8. The vibrational patterns for modes 4, 5, 6, 7, 9, 12, 13, 14, and 15 at the Γ point of SrB_3C at 100 GPa.

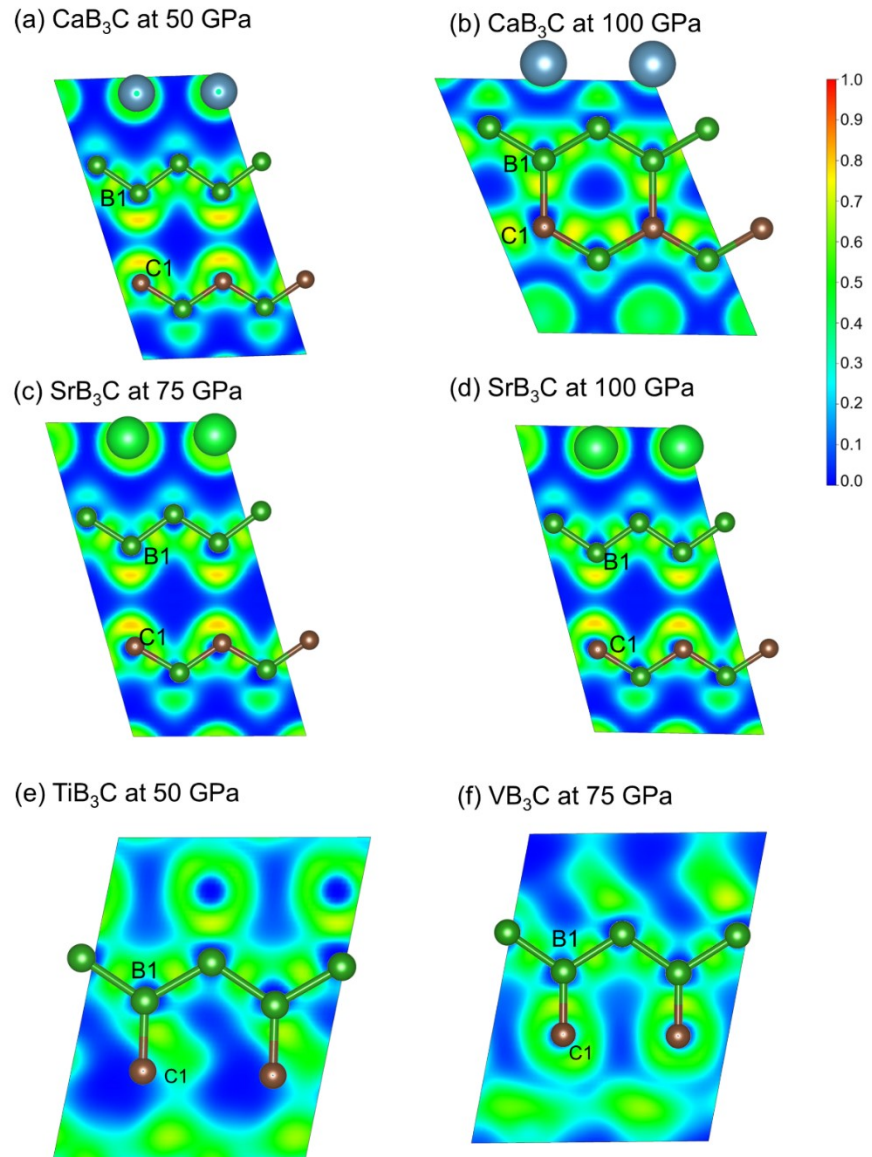


Fig. S9. The electron localization function (ELF) maps of (a) CaB_3C at 50 GPa, (b) CaB_3C at 100 GPa, (c) SrB_3C at 75 GPa, (d) SrB_3C at 100 GPa, (e) TiB_3C at 50 GPa, and (f) VB_3C at 75 GPa.

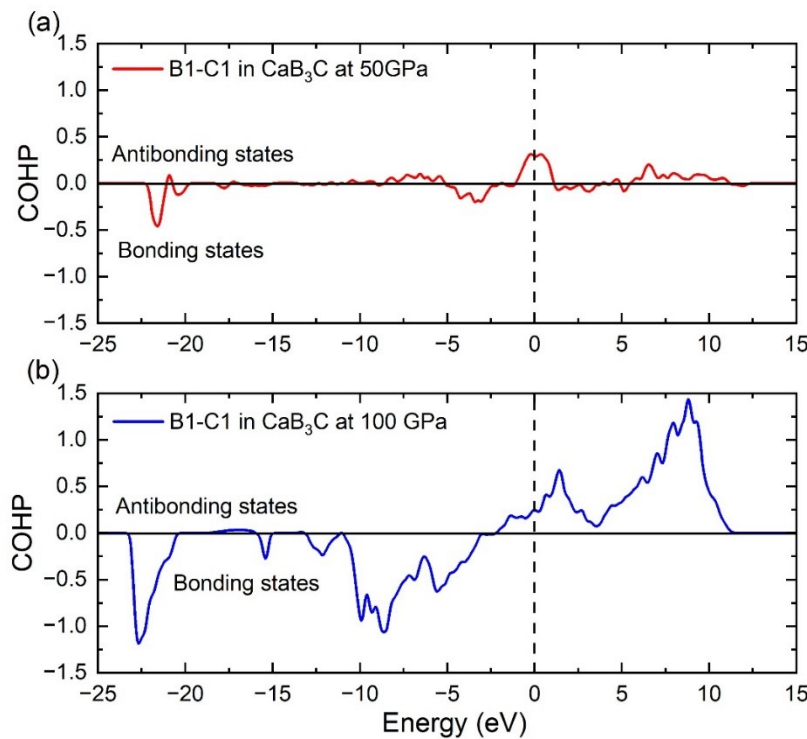


Fig. S10. The COHP for pair B1-C1 in CaB_3C at (a) 50 GPa and (b) 100 GPa.

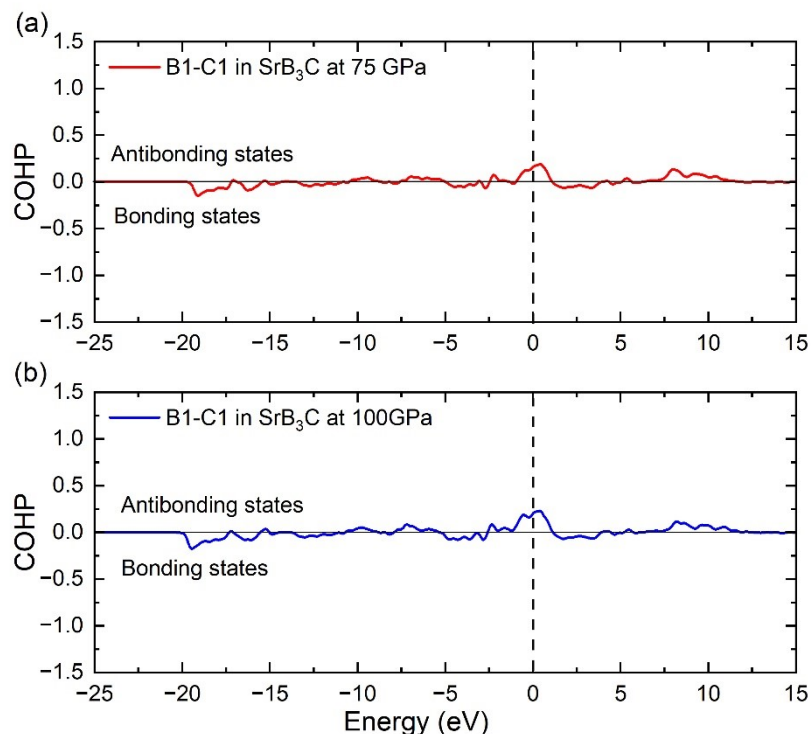


Fig. S11. The COHP for pair B1-C1 in SrB_3C at (a) 75 GPa and (b) 100 GPa.

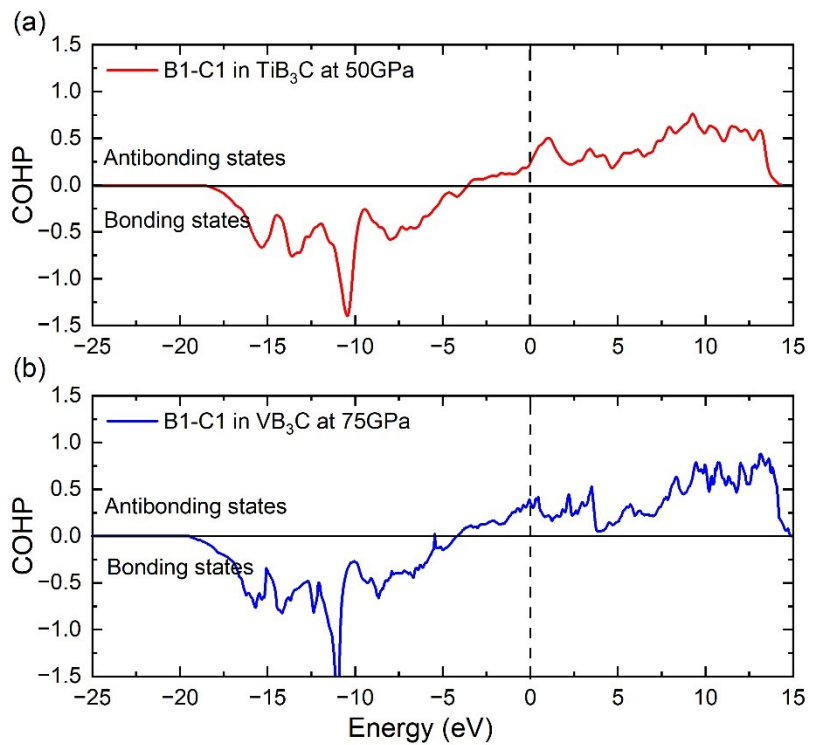
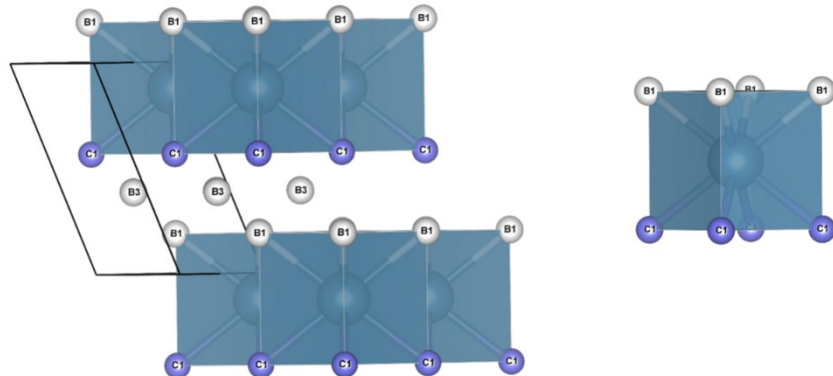


Fig. S12. The COHP for pair B1-C1 in (a) TiB_3C at 50 GPa and VB_3C at 100 GPa.

(a) CaB_3C



(b) SrB_3C

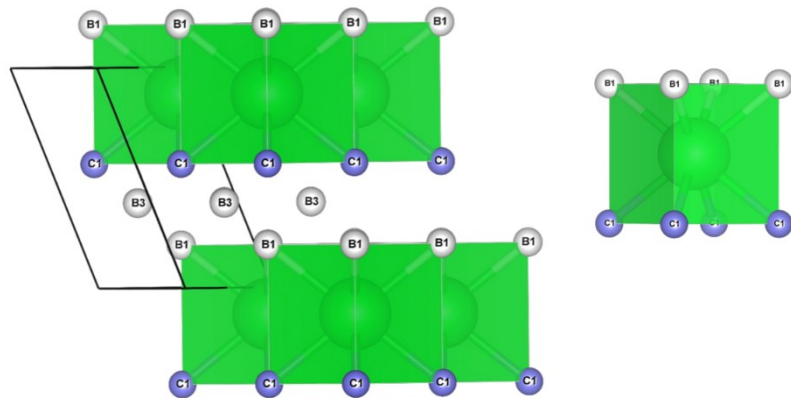
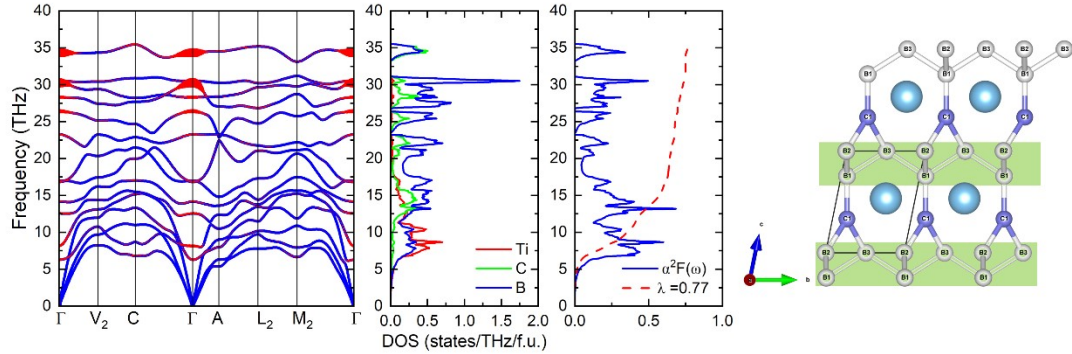


Fig. S13. Crystal structure and coordination polyhedral of (a) CaB_3C and (b) SrB_3C .

(a) TiB_3C at 75 GPa



(b) TiB_3C at 100 GPa

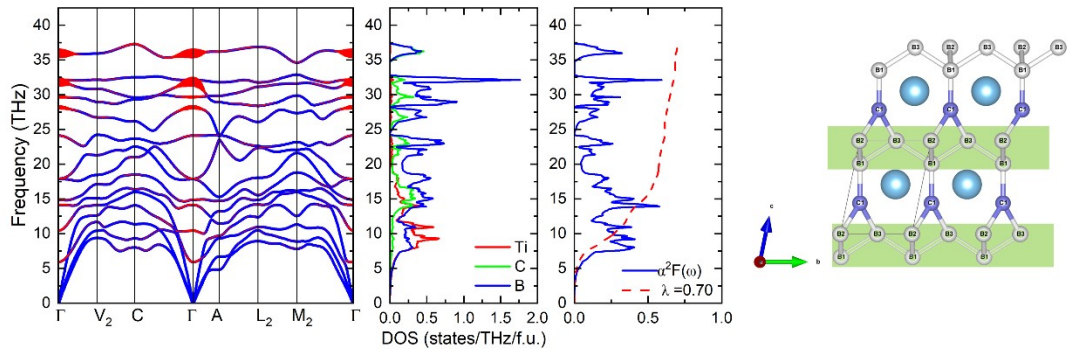


Fig. S14. The γ_{qv} -weighted phonon spectrum, projected phonon density of states (PHDOS), Eliashberg spectral function $\alpha^2F(\omega)$ and crystal structure of TiB_3C at (a) 75 and (b) 100 GPa.

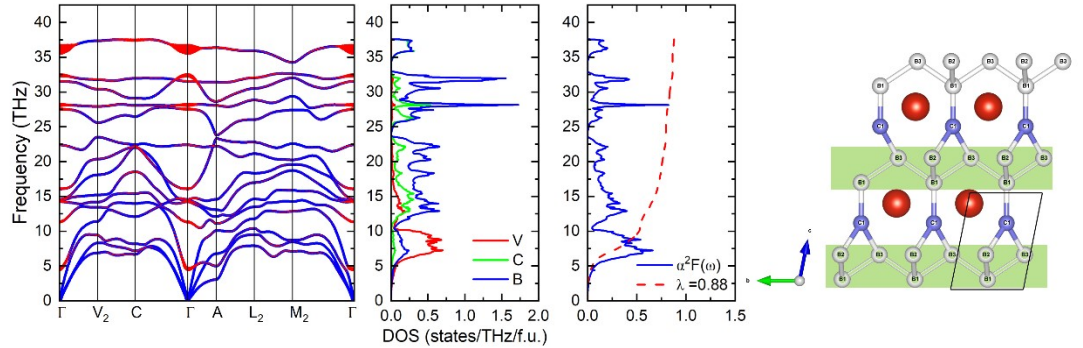


Fig. S15. The γ_{qv} -weighted phonon spectrum, projected phonon density of states (PHDOS), Eliashberg spectral function $\alpha^2F(\omega)$ and crystal structure of VB_3C at 100 GPa.

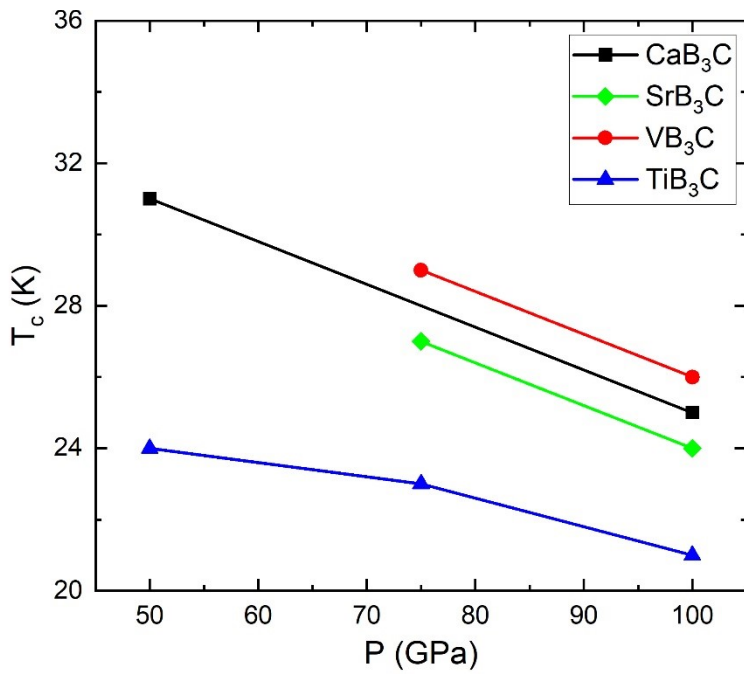


Fig.S16. The pressure-dependence of the T_c of CaB_3C , SrB_3C , TiB_3C , and VB_3C compounds.

Table S1. The covalent radii (\AA) of B and C and ionic radii (\AA) of Ca, Sr, Ti, and V.

	B	C	Ca	Sr	Ti	V
Covalent radii	0.84	0.76				
Ionic radii (8-coordinate)			1.26	1.40	0.88	0.86